

# Spectrally adaptive infrared photodetectors with bias-tunable quantum dots

Ünal Sakoğlu, J. Scott Tyo, and Majeed M. Hayat

*Department of Electrical and Computer Engineering, University of New Mexico, Albuquerque, New Mexico 87131*

Sunil Raghavan and Sanjay Krishna

*Center for High Technology Materials and Department of Electrical and Computer Engineering, University of New Mexico, Albuquerque, New Mexico 87131*

Received May 9, 2003; revised manuscript received August 14, 2003; accepted August 14, 2003

Quantum-dot infrared photodetectors (QDIPs) exhibit a bias-dependent shift in their spectral response. In this paper, a novel signal-processing technique is developed that exploits this bias-dependent spectral diversity to synthesize measurements that are tuned to a wide range of user-specified spectra. The technique is based on two steps: The desired spectral response is first optimally approximated by a weighted superposition of a family of bias-controlled spectra of the QDIP, corresponding to a preselected set of biases. Second, multiple measurements are taken of the object to be probed, one for each of the prescribed biases, which are subsequently combined linearly with the same weights. The technique is demonstrated to produce a unimodal response that has a tunable FWHM (down to  $\Delta\lambda \sim 0.5 \mu\text{m}$ ) for each center wavelength in the range  $3\text{--}8 \mu\text{m}$ , which is an improvement by a factor of 4 over the spectral resolution of the raw QDIP. © 2004 Optical Society of America

OCIS codes: 040.0040, 040.3060, 040.5570, 020.6580, 040.6070, 160.6000, 280.0280.

## 1. INTRODUCTION

Mid-infrared (MIR) sources and detectors, in the wavelength range of  $3\text{--}20 \mu\text{m}$ , are highly desirable for many varied applications such as night-vision cameras, mine-detection systems, thermal imaging, chemical analysis, and effluent detection. However, the technology for the fabrication of spectral detectors in this wavelength range has been plagued with several problems. One of the biggest drawbacks of the present-day MIR detectors is their inability to operate at air-cooled temperatures ( $T = 190\text{--}200 \text{ K}$ ), although they demonstrate favorable device performance at cryogenic temperatures ( $T = 40\text{--}80 \text{ K}$ ).

There are presently three different material systems and technologies that are being pursued to realize MIR photonic detectors. Low-bandgap materials, such as HgCdTe,<sup>1,2</sup> are the current state of the art detectors due to their high responsivity and detectivity ( $D^*$ ). However, there remain problems in the epitaxial growth of HgCdTe-based materials due to the presence of large interface instabilities and etch-pit and void-defect densities, and this is reflected in the high uncertainties and fluctuations in the value of  $D^*$ .<sup>3</sup> One alternative to direct bandgap detectors is the use of type II strained-layer superlattice with materials such as InAsSb–InSb or InGaSb–InAs.<sup>4,5</sup> But the epitaxial-growth technique for the antimonides is also not very mature and reliable either, due to group V intermixing during growth. Moreover, surface passivation is also a big concern for antimonide-based devices.

Alternatively, devices based on intersubband transitions in quantum-confined heterostructures in III–V com-

pounds can be used for MIR detection.<sup>6–11</sup> The optical transitions in these devices could involve subband-to-subband or subband-to-continuum transitions. The advantage of this approach is that it is based on a mature fabrication technology, leading to higher uniformity in structures and lower cost. One such device, based on intersubband transitions in quantum wells, is called the quantum-well infrared photodetector<sup>7</sup> (QWIP). QWIPs have demonstrated efficient detection in the spectral range of  $3\text{--}20 \mu\text{m}$  and can be tuned by varying the quantum-well width and material systems. However, these devices have shortcomings due to certain intrinsic factors. First, the selection rules of the intersubband transitions prevent normal-incidence photons from being absorbed by transitions from the ground state to the excited state.<sup>7</sup> Second, because of the very short lifetime of electrons in the excited state ( $\sim 5 \text{ ps}$ ), the electrons relax back to the ground state before they can escape from the quantum well and contribute to the photocurrent. As a consequence, the detectivity,  $D^*$ , and the quantum efficiency of these devices are low at room temperature.<sup>12</sup> To overcome the first limitation, patterned surfaces or waveguide structures are employed.<sup>9</sup> To minimize the deleterious effects arising from the second factor, the devices need to be cooled to liquid-nitrogen temperatures.<sup>7</sup> Recent comparisons among the present-day technologies for MIR detection have been presented by Kinch<sup>13</sup> and Rogalski.<sup>14</sup>

Recently, normal-incidence MIR detection in the range of  $5\text{--}17 \mu\text{m}$  has been demonstrated with intersubband transitions in self-organized quantum dots.<sup>15–17</sup> Quantum-dot (QD) detectors are expected to demonstrate

good performance at elevated temperatures, due to their favorable carrier dynamics.<sup>18,19</sup> The theoretically obtained dark current in quantum-dot detectors is much lower compared with the dark current in QWIPs, primarily due to the large intersubband relaxation time in the dots.<sup>20</sup> The main contribution to the dark current arises from the large thermionic emission in these dots.

For many applications in infrared remote sensing, it is desirable to have a spectrally tunable response. With such a capability, the response of a focal-plane array (FPA), for example, can be tuned to aid in the detection of a particular type of target, optimized for use under particular imaging scenarios, or even used to generate multispectral or hyperspectral images, which have the spectral radiance sampled at many wavelengths at *each* pixel in a scene (as the pixel is spectrally tuned in time). Regardless of the specific application, spectral tunability is traditionally obtained with some optical or electro-optical technique.

Indeed, the most primitive (and generally the simplest and cheapest) method for obtaining multispectral images (with typically 3–15 spectral bands) is through the use of spectral filters in front of the focal plane. The various spectral images can be collected sequentially in time, by use of the same focal plane and switching filters between images, or by simultaneous use of multiple focal planes. Hyperspectral sensors (with upwards of 100 spectral bands) typically use some sort of a shearing optic (such as a grating or prism) to separate the light incident on the sensor into either spectral or interferometric paths. One dimension of the FPA is typically used to collect the spectral data, and the second dimension is used to collect a line image. The second spatial dimension is obtained through scanning. Other strategies have been used that instantaneously collect all of the spectral data by sacrificing spatial resolution through the subdivision of the array into targets where temporal scanning can produce motion artifacts.

Recently, efforts have been made to allow a single FPA to be electronically tuned to be sensitive in two or more regions of the spectrum. Such cameras are often referred to as two-color cameras, with sensitivity at two different wavelengths in, for example, the long-wave infrared (8–12  $\mu\text{m}$ ).<sup>22</sup> Such strategies provide for greater optical simplicity because the spectral response is controlled electronically rather than through optics. This electronic tunability provides for multifunction utility of the FPA (two-color, one-color, etc). However, most existing sensors are limited in that the spectral sensitivity can be electronically *switched* but not continuously tuned. Furthermore, while the center wavelength can sometimes be tuned, the spectral resolution in each tuned state is usually fixed.

In this paper, we present a continuously tunable infrared FPA pixel technology. This technology combines electronically tunable quantum-dot infrared photodetectors (QDIPs) with signal-processing strategies that allow both the center wavelength *and* spectral resolution to be independently chosen (within certain limits) in the mid- to long-wave infrared regime (3–8  $\mu\text{m}$ ). The ability to continuously and independently tune both the center wave-

length and the spectral resolution will allow this pixel technology to be incorporated into cameras for a variety of tasks. Potential applications include adaptive multispectral imagery and spectrally tailored panchromatic imagery.

## 2. QUANTUM-DOT INFRARED PHOTODETECTORS

### A. Structures and Basic Principles

Although it has been known for a long time that the discrete atomlike density of states present in quantum dots would lead to significant improvements in device performance, the technology to fabricate these extremely small objects did not exist in the laboratory until recently. For room-temperature operation of these devices, the largest dimension of the dots has to approach 15–20 nm. Such small structures are extremely difficult to fabricate with conventional lithography techniques since the process-induced defects render the QDs optically dead.<sup>23</sup> An extremely promising approach that has emerged over the past decade is based on the creation of *self-assembled quantum dots* by highly strained epitaxial growth.<sup>24</sup> Under certain growth conditions, the epitaxial film thermodynamically prefers to minimize its free energy by assembling into three-dimensional islands instead of forming a

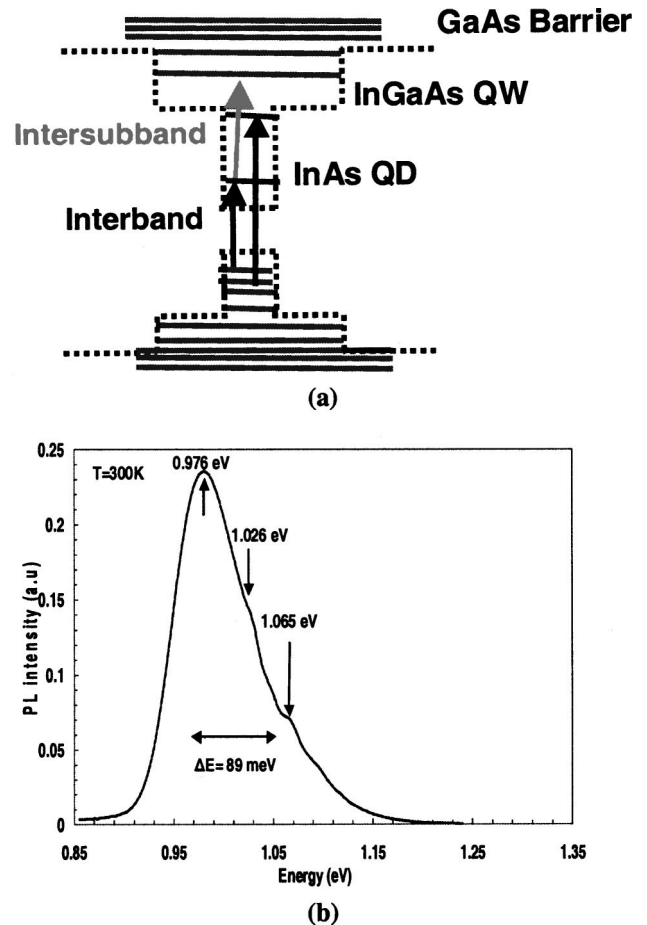


Fig. 1. (a) Band structure and (b) room-temperature photoluminescence for a 10-layer InAs/In<sub>0.15</sub>Ga<sub>0.85</sub>As DWELL heterostructure.

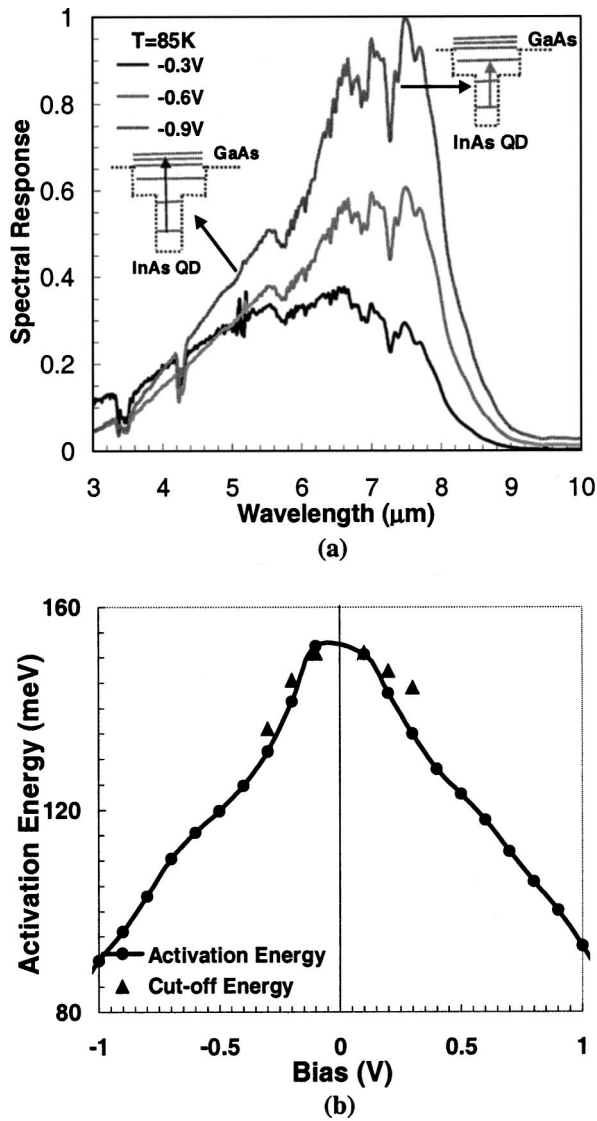


Fig. 2. Bias-dependent (a) spectral response and (b) activation energy for a 10-layer InAs/In<sub>0.15</sub>Ga<sub>0.85</sub>As DWELL detector. The cut-off energy is also shown in (b). The structures on the spectra are not fluctuations but rather reflect the atmospheric absorption over this wavelength range.

two-dimensional layer. These self-assembled islands, also known as quantum dots, are typically pyramid to lens shaped with lateral dimensions of 15–20 nm and vertical dimension of 7–8 nm. These structures can be formed from important semiconductor systems such as InGaAs/GaAs, SiGe/Si, and InGaAs/InP.

Since the intersubband energy spacing in the QDs lies in the mid-infrared range (5–20  $\mu\text{m}$ ), they can be used to fabricate long-wavelength sources and detectors. The long carrier relaxation times in QDs, possibly due to the presence of the phonon bottleneck, could be exploited to increase the operating temperatures of these detectors. The long relaxation time in quantum dots ensures that the photogenerated carriers stay at the excited state for a longer time and contribute more efficiently to the photocurrent.<sup>18,19</sup>

Most of the QD detectors reported so far have InAs or InGaAs dots sandwiched in a GaAs matrix. Recently, we

have been investigating heterostructures in which InAs dots are placed in a thin InGaAs quantum well. This structure, also known as dots-in-a-well (DWELL) design, is being used widely to fabricate low-threshold, high-power QD lasers operating at 1.3  $\mu\text{m}$ .<sup>25</sup> The presence of the InGaAs well in the DWELL design lowers the ground state of the dot, thus increasing the effective barrier seen by the carriers. This is expected to lead to a lower thermionic emission and a higher operating temperature for the intersubband QD detector. Moreover, DWELL dots are found to have a larger areal density, which could lead to increased responsivity. The band structure of the DWELL design along with room-temperature photoluminescence is shown in Fig. 1.

## B. Spectral Response and its Bias-Dependent Shift

Figure 2(a) shows the normal-incidence spectral response obtained from a 10-layer InAs/In<sub>0.15</sub>Ga<sub>0.85</sub>As structure at 78 K for different bias voltages. The details of the device design and fabrication are discussed elsewhere.<sup>17</sup> The peak of the response is approximately at 7.2  $\mu\text{m}$  (170 meV) with a spectral width ( $\Delta\lambda/\lambda$ ) of 35% ( $\Delta\lambda = 2.5 \mu\text{m}$ ). Such a broad response is a desirable feature for long-wave infrared detectors, as they provide a wide spectral coverage. (Note that the patterns on the spectra reflect the atmospheric absorption over this wavelength range.) It is interesting to note that the cut-off energy obtained from the spectral-response measurement (8.2  $\mu\text{m}$  or 151 meV at a bias voltage  $V_b = -0.1 \text{ V}$ ) agrees very well with the activation energy extracted from the dark-current measurements ( $\sim 152 \text{ meV}$ ,  $V_b = -0.1 \text{ V}$ ), as shown in Fig. 2(b). Moreover, both of them display a red shift at increased values of the applied bias due to band-bending effects.

The energy difference between the position of the ground state of the dot and the position of the GaAs band edge from the photoluminescence spectrum [see Fig. 1(a)] is found to be 424 meV. In accordance with the analysis by Kim *et al.*,<sup>26</sup> the sum of binding energies for the electrons and holes can be estimated to be 424 meV. Realizing that the electron-binding energy is much larger than the hole-binding energy, the difference between the conduction band edge of GaAs and ground state of the dot is expected to be greater than 212 meV. Hence we believe that the peak at 7.2  $\mu\text{m}$  (172 meV, which is less than 212 meV) is due to a bound-to-bound transition between the ground state of the dot and states within the In<sub>0.15</sub>Ga<sub>0.85</sub>As quantum well, whereas the broad shoulder observed around 5  $\mu\text{m}$  (248 meV, which is greater than 212 meV) is due to the bound-to-continuum transition, as depicted in the inset to Fig. 2(a).

By varying the thickness and composition of the InGaAs well and the surrounding barrier layers, the operating wavelength of the detector can be tuned over the mid- to long-wave infrared regime. Once we fix the operating wavelength of the detector, further tuning within the wave band can be accomplished by varying the bias of the detector. Figure 3 shows the variation of the peak operating wavelength (obtained from a Gaussian fit to the data) as a function of the applied bias. It is seen that there is a definite dependence of the peak wavelength on the operating bias.



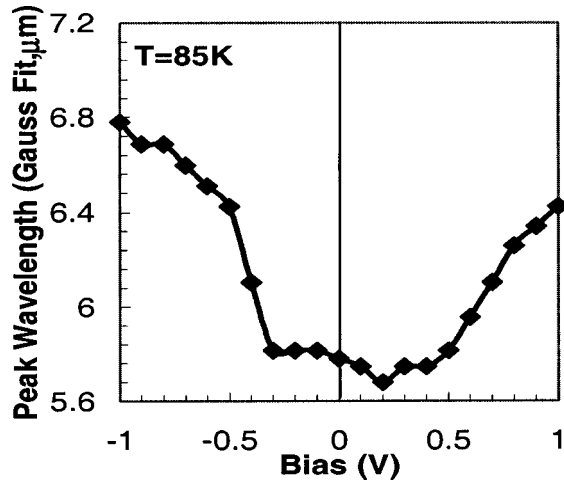


Fig. 3. Variation of the peak operating wavelength (from a Gaussian fit) from a 10-layer InAs/In<sub>0.15</sub>Ga<sub>0.85</sub>As DWELL detector as a function of the applied bias.

### 3. POSTPROCESSING ALGORITHM FOR SPECTRAL ADAPTIVITY

As seen from Fig. 2, there is a significant overlap between the spectra obtained at different biases, and the response at each individual bias is spectrally broad. This broad spectral coverage, which is very advantageous for the broadband imaging applications, proves to be disadvantageous for applications that require narrow spectral resolution. However, by use of a novel algorithm-based postprocessing technique, the bias-driven diversity in the spectra can be exploited to produce an approximately unimodal response that can be tuned from 5–8  $\mu\text{m}$  and has a tunable FWHM (down to  $\Delta\lambda \sim 0.5 \mu\text{m}$ ) for each center wavelength, which is an improvement by a factor of 4 over the spectral resolution of the quantum-dot infrared detector (QDIP) alone.<sup>27</sup> Other spectral-response characteristics can also be accommodated with the same postprocessing technique. This technique, which is the main contribution of the paper, is described below.

#### A. Algorithm Development

Suppose that we are interested in a detector with a specific desired spectral response. The proposed postprocessing technique for achieving this desired response can be summarized in the following two steps: First, we approximate the desired spectral response, as a function of the wavelength  $\lambda$ , by the “best” weighted superposition of a family of bias-controlled spectra of the QDIP detector, corresponding to a preselected set of bias voltages. This step is referred to henceforth as the “projection step,” and it is shown schematically in Fig. 4(a). Second, we take multiple QDIP measurements of the object to be probed, one for each of the prescribed bias voltages, and form a superposition of the measurements according to the weights calculated in the projection step. The entire postprocessing technique is schematically shown in Fig. 4(b).

We now turn to the mathematical justification of the algorithm. Let  $R_V(\lambda)$  denote the spectral response of a QDIP detector when the detector is biased by  $V$  volts, and suppose that the spectrum  $R_V(\lambda)$  has been measured *a*

*priori* for  $M$  voltages,  $V_1, \dots, V_M$ . Now let  $R(\lambda)$  denote the desired spectral response, which is assumed to be in the range  $\lambda_{\min}$  to  $\lambda_{\max}$ . Suppose that  $M$  measurements,  $Y_1, \dots, Y_M$ , of a radiating object are collected with the QDIP, where  $Y_i$  is obtained at an applied bias  $V_i$ . The goal of the postprocessing algorithm is to seek a set of weights  $w_1, \dots, w_M$ , depending on  $R$ , so that the superposition response

$$\hat{Y} = \sum_{i=1}^M w_i Y_i \quad (1)$$

“best” approximates the response  $Y$ , which we would have measured had the detector possessed the desired spectral response  $R(\lambda)$ . As commonly practiced in signal process-

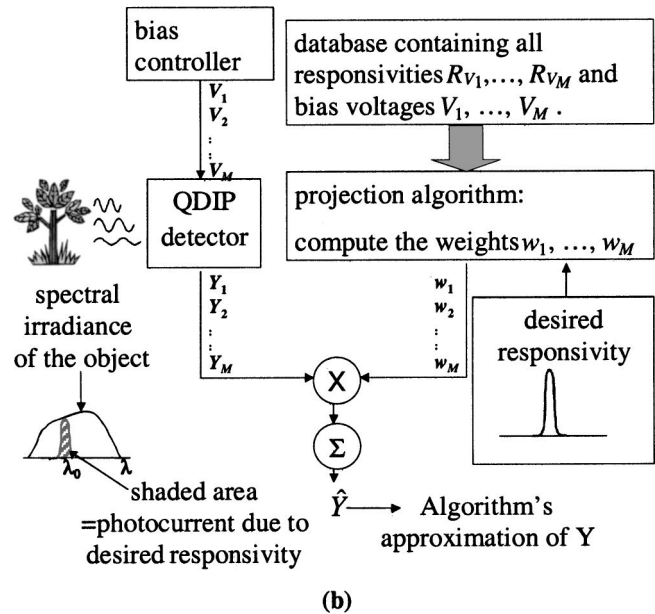
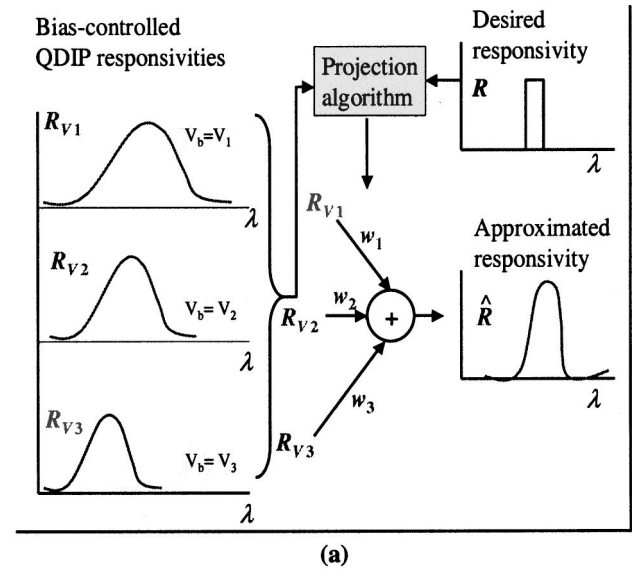


Fig. 4. (a) Schematic of the projection step: approximation of any desired responsivity by forming an optimal linear superposition of the QDIP responsivities at different biases. (b) Schematic of our reconstruction algorithm, combining the bias-dependent output from the QD sensors to get the desired responsivity.

ing, we will pursue the approximation in the sense of minimizing the mean-square error  $|\hat{Y} - Y|^2$ . In particular, we seek the set of weights, written in vector form as

$$\mathbf{w} = [w_1, \dots, w_M]^T, \quad (2)$$

which minimizes the error  $|\hat{Y} - Y|^2$ . We show below that a solution to this minimization problem can be equivalently obtained by determining the set of weights that minimizes the integrated mean-square error

$$\epsilon(R; M) = \int_{\lambda_{\min}}^{\lambda_{\max}} \left| \sum_{i=1}^M w_i R_{V_i}(\lambda) - R(\lambda) \right|^2 d\lambda, \quad (3)$$

which is associated with approximating the desired spectral response  $R(\lambda)$  by

$$\hat{R}(\lambda) = \sum_{i=1}^M w_i R_i(\lambda). \quad (4)$$

This assertion can be justified as follows: First, note that the measurement  $Y$  is proportional to the integral  $\int_{\lambda_{\min}}^{\lambda_{\max}} G(\lambda) R(\lambda) d\lambda$ , where  $G(\lambda)$  is the infrared spectral radiance at the detector's active surface. Now the error  $|\hat{Y} - Y|^2$  can be cast as

$$\begin{aligned} |\hat{Y} - Y|^2 &= \left| \int_{\lambda_{\min}}^{\lambda_{\max}} G(\lambda) \left[ R(\lambda) - \sum_{i=1}^M w_i R_{V_i}(\lambda) \right] d\lambda \right|^2 \\ &\leq \left\{ \int_{\lambda_{\min}}^{\lambda_{\max}} \left| G(\lambda) \left[ R(\lambda) - \sum_{i=1}^M w_i R_{V_i}(\lambda) \right] \right|^2 d\lambda \right\}^2. \end{aligned}$$

The last integral can be further upper bounded with the Schwarz inequality<sup>28</sup> so that

$$\begin{aligned} |\hat{Y} - Y|^2 &\leq \left[ \int_{\lambda_{\min}}^{\lambda_{\max}} G^2(\lambda) d\lambda \right] \left\{ \int_{\lambda_{\min}}^{\lambda_{\max}} \left[ R(\lambda) - \sum_{i=1}^M w_i R_i(\lambda) \right]^2 d\lambda \right\}. \end{aligned} \quad (5)$$

Thus if we consider (without loss of generality) a normalized irradiance function  $G$  so that the first integral is unity, then minimizing the maximum of  $|\hat{Y} - Y|^2$  over all possible normalized radiance functions  $G$  amounts to minimizing the second integral in Eq. (5), which proves the assertion leading to the integral in Eq. (3). The requirement that we should minimize the maximum (over all possible normalized radiance functions  $G$ ) of the error  $|\hat{Y} - Y|^2$  is reasonable since the choice of the weights should not depend on the unknown irradiance function  $G$  and the approximation should be accurate uniformly in  $G$ . If there is some knowledge of the distribution of  $G$  in a particular application, this can be used to improve the performance. Finally, the integrated error given in Eq. (3) can be discretized and the weight vector,  $\mathbf{w}$ , can be analytically determined with standard quadratic minimization techniques. The details of computing the vector  $\mathbf{w}$  (comprising the projection step) are given in Subsection 3.C.

We emphasize that in the spectral approximation shown in Eq. (4), the shape, width, and center wavelength of  $R$  is arbitrary. Thus the proposed postprocessing tech-

nique can be designed to synthetically tune the detector's response to an arbitrary center wavelength and spectral width. Clearly, to obtain good results, the approximation error between the ideal responsivity  $R(\lambda)$  and its approximation  $\hat{R}(\lambda)$  must be small. Thus the choice of the desired spectral width and the center wavelength must be compatible with the range of the wavelengths covered by the ensemble of bias-dependent spectral responses.

### B. Regularized Version of the Algorithm

In the above projection-based development of the approximate spectral response  $\hat{R}(\lambda)$ , no smoothness constraint was imposed on  $\hat{R}(\lambda)$ . In practical situations, however, the resulting  $\hat{R}(\lambda)$  may be undesirably rough, despite the fact that it achieves the minimum mean-square error. This roughness is partially attributable to the high-frequency content of the bias-dependent spectra themselves, which is due to the sharp transitions in the spectra at the atmospheric-absorption bands. It can also result from requiring stringent FWHM and tuning requirements, which would result in the significant amplification of certain segments of the spectra that may contain a high level of fluctuation. To remedy this problem, a smoothness criterion can be built into the minimization (over  $\mathbf{w}$ ) of the error given by Eq. (3). This will bring smoothness to  $\hat{R}(\lambda)$  at the tolerable expense of reduced spectral resolution. To do so, we introduce the regularized mean-square error

$$\begin{aligned} \epsilon(R; M; \alpha) &= \int_{\lambda_{\min}}^{\lambda_{\max}} \left\{ \left| \sum_{i=1}^M w_i R_{V_i}(\lambda) - R(\lambda) \right|^2 \right. \\ &\quad \left. + \alpha \left[ \frac{d^2}{d\lambda^2} \sum_{i=1}^M w_i R_{V_i}(\lambda) \right]^2 \right\} d\lambda, \end{aligned} \quad (6)$$

where the Laplacian operator,  $d^2/d\lambda^2$ , is used to measure roughness in the approximation. The regularization parameter,  $\alpha \geq 0$ , controls the amount of penalization imposed on the roughness. Its specific value is typically chosen according to the user's experience. (In our calculations the value  $\alpha = 0.04$  gave good results). As before, the above regularized error can be discretized and the weight vector  $\mathbf{w}$  can be solved for analytically. The details of the calculation of the weight vector  $\mathbf{w}$  [which minimizes the regularized error in Eq. (6)] are considered next.

### C. Numerical Implementation of the Algorithm

We now proceed to determine the weight vector  $\mathbf{w}$ . Upon discretizing (in the variable  $\lambda$ ) the integral in Eq. (6), the integrated mean-square error can be approximated by the discrete sum

$$\begin{aligned} \epsilon(R; M; \alpha) &\approx \Delta\lambda L^{-1} \sum_{k=1}^L \left[ R(\lambda_k) - \sum_{i=1}^M w_i R_i(\lambda_k) \right]^2 \\ &\quad + \alpha \left[ \sum_{i=1}^M w_i [-R_i(\lambda_{k-1}) + 2R_i(\lambda_k) \right. \\ &\quad \left. - R_i(\lambda_{k+1})] \right]^2, \end{aligned} \quad (7)$$

where  $\Delta\lambda = \lambda_{\max} - \lambda_{\min}$ ,  $\lambda_1 = \lambda_{\min}$ , ...,  $\lambda_L = \lambda_{\max}$ ,  $\lambda_{k+1} - \lambda_k = \Delta\lambda/L$ , and  $L$  is the mesh size (total wave bins)

used in approximating the integral. If we define the vector  $\mathbf{R} = [R(\lambda_1) \cdots R(\lambda_L)]^T$  and form the matrix

$$\mathbf{A} = \begin{bmatrix} R_{V_1}(\lambda_1) & R_{V_2}(\lambda_1) & \cdots & R_{V_M}(\lambda_1) \\ R_{V_1}(\lambda_2) & R_{V_2}(\lambda_2) & \cdots & R_{V_M}(\lambda_2) \\ \vdots & \vdots & \ddots & \vdots \\ R_{V_1}(\lambda_L) & R_{V_2}(\lambda_L) & \cdots & R_{V_M}(\lambda_L) \end{bmatrix}, \quad (8)$$

we can recast the integrated error in Eq. (6) in matrix form as

$$\epsilon(\mathbf{R}; \mathbf{M}, \alpha) \equiv \Delta \lambda L^{-1} [\|\mathbf{R} - \mathbf{A}\mathbf{w}\|^2 + \alpha \|\mathbf{Q}\mathbf{A}\mathbf{w}\|^2], \quad (9)$$

where  $\mathbf{Q}$  is the Laplacian operator matrix corresponding to the weighting operation in Eq. (6). ( $\mathbf{Q}$  is an  $L$ -by- $L$  matrix, where each entry on the main diagonal is “2” and the first subdiagonal and superdiagonals entries are “-1.”) From basic quadratic minimization principles,<sup>29</sup> the weight vector  $\mathbf{w}$  can be found with the following simple formula, which actually gives the projection of the spectrum  $R$  onto the finite-dimensional function space spanned by the spectra  $R_1, \dots, R_M$ :

$$\mathbf{w} = (\mathbf{A}^T \mathbf{A} + \alpha \mathbf{A}^T \mathbf{Q}^T \mathbf{Q} \mathbf{A})^{-1} \mathbf{A}^T \mathbf{R}, \quad (10)$$

where the superscript “ $T$ ” denotes the matrix transpose operator. Thus the desired superposition of measurements, shown in Eq. (1), can now be computed with the weight coefficient provided  $\mathbf{w}$  [as schematically shown in Fig. 4(b)].

#### 4. EXPERIMENTAL RESULTS

Two separate QDIPs (which we refer to in this paper as QDIP 1198 and QDIP 1199) were fabricated with the same methods described by Rotella *et al.*<sup>30</sup> The sets of biased-dependent responses for these two devices were measured and subsequently used in the postprocessing technique to generate simulated tuned responses with varying FWHMs and center wavelengths. The two devices have slightly different responses, as shown in Fig. 5.

Figure 6 shows examples of simulated tuned responses for narrow (0.5  $\mu\text{m}$ ), medium (1.0  $\mu\text{m}$ ), and coarse (3.0  $\mu\text{m}$ ) spectral resolution at various center wavelengths across the sensitivity range of the QDIPs. In computing the spectral-response functions for QDIP 1198, twenty biases were used ( $M = 20$ ) for which  $[V_1, \dots, V_{20}] = [-1, -0.9, \dots, -0.1, 0.1, \dots, 0.9, 1]$  V. For QDIP 1199, on the other hand,  $M = 21$  and  $[V_1, \dots, V_{21}] = [-1, -0.9, \dots, 0, \dots, 0.9, 1]$  V.

Figures 7(a) and 7(b) show the variation in the spectral resolution (viz., FWHM) rendered by the postprocessing algorithm as the tuning wavelength ( $\lambda_0$ ) and the desired FWHM are changed for the two different QDIPs. For each selection of the tuning parameter and desired FWHM, the shape of the desired response is taken as a triangular function, whose base is twice as wide as the desired FWHM. Note that as we move up the vertical axis scale, the resulting FWHM rendered by the postprocessing algorithm decreases. Hence the highest regions represent the narrowest FWHM. The transparent planes in the figures represent spectral resolution of 1  $\mu\text{m}$  (recall

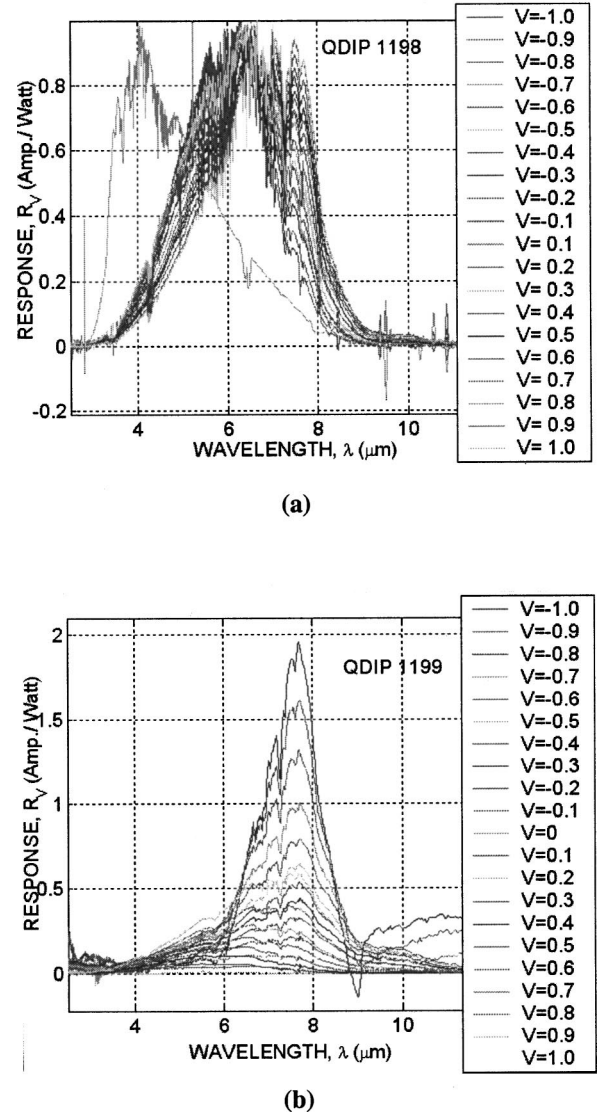


Fig. 5. Bias-dependent spectral response of (a) QDIP 1198 (b) QDIP 1199. The numbers in the legends correspond to the applied bias voltages (volts) of the detectors.

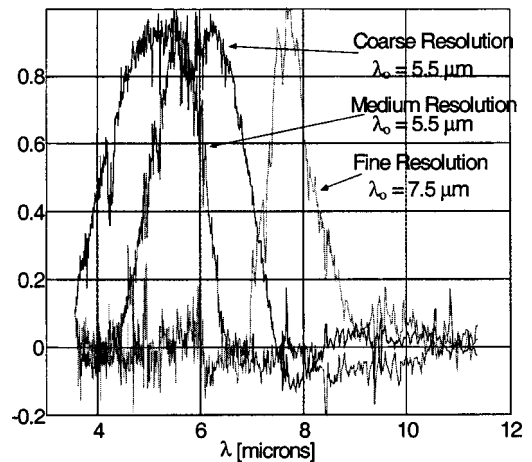


Fig. 6. Examples of the simulated tuned (normalized) responsivity generated by the postprocessing technique. Three responsivities are shown corresponding to wide (3.0  $\mu\text{m}$ ), medium (1.0  $\mu\text{m}$ ), and narrow (0.5  $\mu\text{m}$ ) FWHMs at different center wavelengths  $\lambda_0$ .



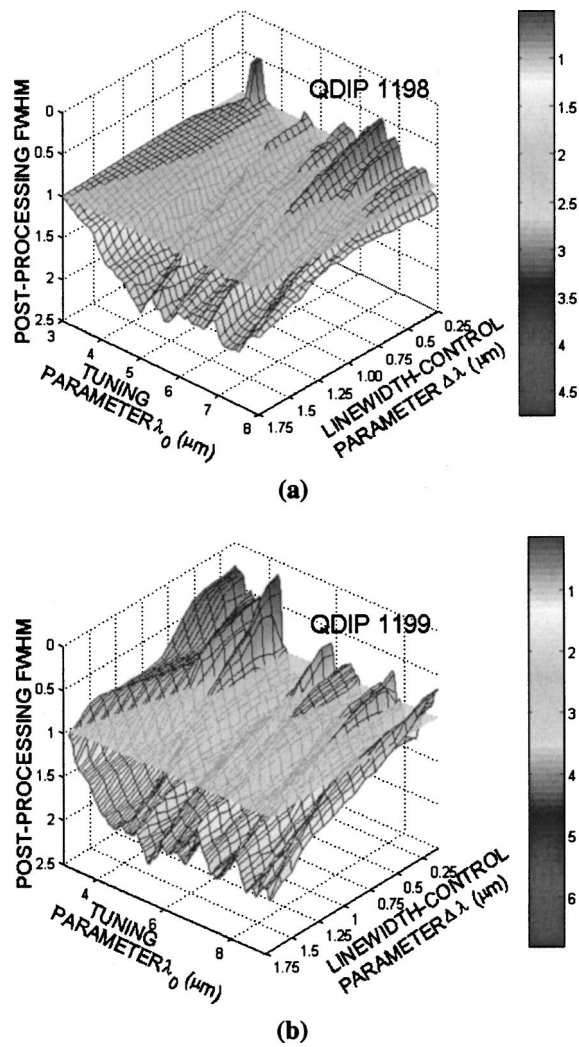


Fig. 7. Attained spectral resolution (FWHM) as a function of desired center wavelength and spectral bandwidth (linewidth parameter): (a) for the two QDIP 1198; (b) QDIP 1199 detectors reported in Ref. 31. Note that the vertical axis is inverted, so the *highest* spectral resolution (lowest line width) is at the top.

that the FWHM associated with QDIPs' spectral response is in excess of  $2 \mu\text{m}$ ). Moreover, the data in Fig. 8 indicate that spectral resolution of the order of  $0.5 \mu\text{m}$  can be obtained continuously across the wavelength range of  $3\text{--}8 \mu\text{m}$  for both detectors. Also, the spectral resolution can be tuned from  $0.5 \mu\text{m}$  to over  $3.0 \mu\text{m}$  regardless of center wavelength. For both QDIPs, a FWHM of  $\sim 0.5 \mu\text{m}$  is the practical lower limit that we are able to obtain in these examples.

#### A. Demonstration of Spectral Adaptivity

In order to demonstrate the potential of the spectrally adaptive QDIPs, we have performed experiments to predict the performance in a variety of spectral-sensing modes. We tested the ability of the QDIP technology to differentiate the transmission spectrum of a  $76.2\text{-}\mu\text{m}$ -thick polystyrene sheet from a blackbody spectrum obtained from a global source. The QDIPs were operated as a hyperspectral sensor, a seven-band multispectral sensor, and a three-band multispectral sensor. The parameters of each of the spectral sensing modes is pre-

sented in Table 1, including the number of spectral bands and desired spectral resolution of each band.

For each spectral-sensing mode, the parameters in Table 1 were supplied to the postprocessing algorithm described above. The weights necessary to realize each spectral band were computed based on the measured re-

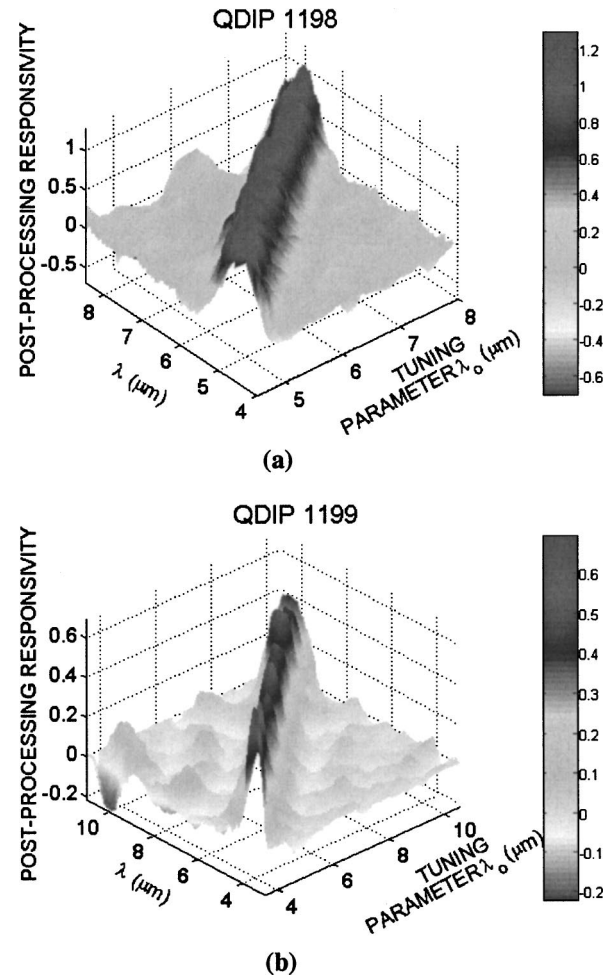


Fig. 8. Spectral response at a desired linewidth (FWHM) of  $0.5 \mu\text{m}$  as a function of desired center frequency for the two QDIP detectors reported in Ref. 31. A band with FWHM  $< 1 \mu\text{m}$  can be achieved for most of the tuning parameter values (center wavelength) of  $3\text{--}8 \mu\text{m}$ , especially for the QDIP 1199 device. For the tuning parameter values between  $3.0$  and  $4.5$  with the QDIP 1199 device, FWHM  $< 0.5$  can be achieved [also see Fig. 7(b)].

Table 1. Parameters Used for the Three Simulated Sensing Modes

Mode	Number of Bands	Band Centers	Desired Resolution
Hyperspectral	200	$3.5\text{--}10.5 \mu\text{m}$ (every $0.05 \mu\text{m}$ )	$0.5 \mu\text{m}$
Multispectral	7	$4\text{--}10 \mu\text{m}$ (every $1 \mu\text{m}$ )	$1 \mu\text{m}$
Multispectral	3	$5 \mu\text{m}$	$2 \mu\text{m}$
		$7.5 \mu\text{m}$	$1 \mu\text{m}$
		$9.5 \mu\text{m}$	$2 \mu\text{m}$

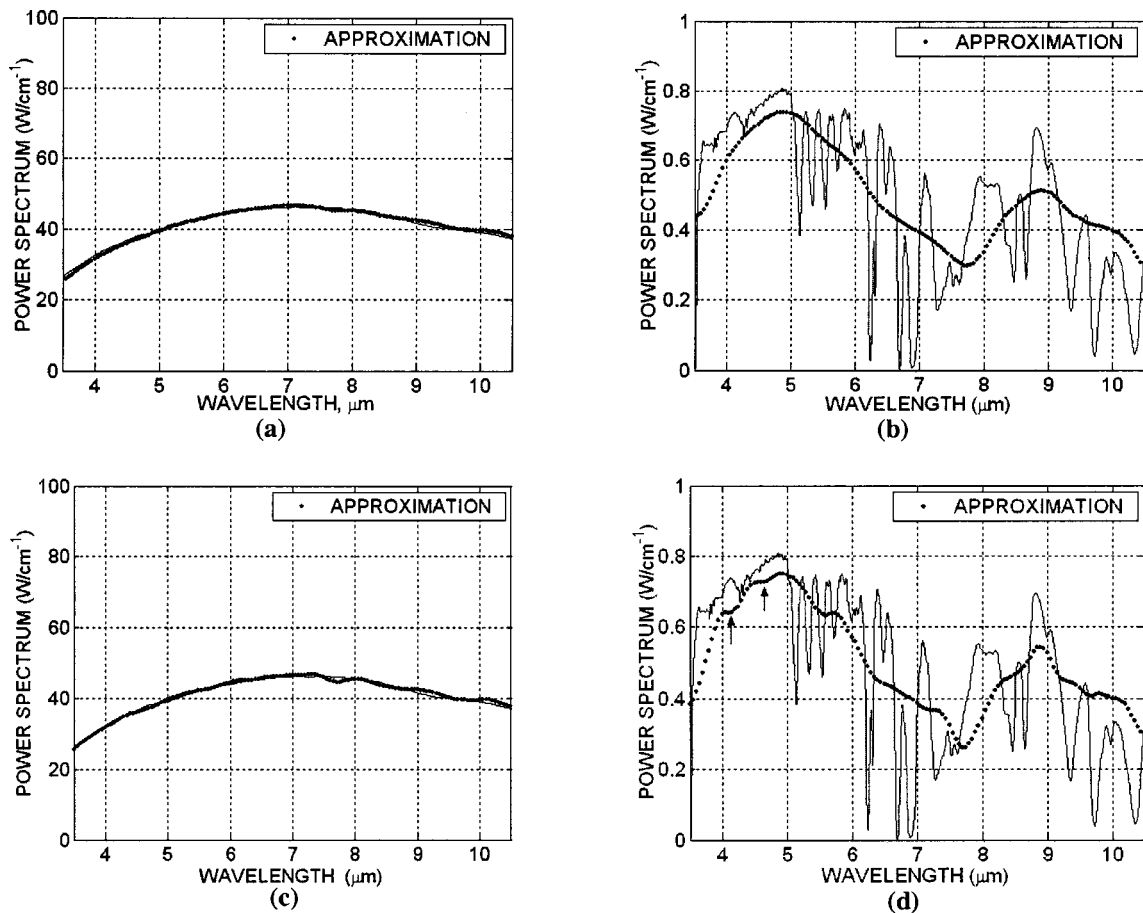


Fig. 9. Spectral reconstruction with the algorithm: (a) Reconstruction of blackbody spectrum by use of triangular filters of parameter (FWHM)  $0.5 \mu\text{m}$ . (b) Reconstruction of 3-mm polystyrene spectrum by use of triangular filters of parameter (FWHM)  $0.5 \mu\text{m}$ . (c) Same as (a) but with FWHM =  $0.25 \mu\text{m}$ . (d) Same as (b) but with FWHM =  $0.25 \mu\text{m}$ .

sponse spectral, and the resulting spectral-sensitivity functions were computed through linear combination of the photocurrents corresponding to the various biases. The photocurrent of the QDIP at each bias value was obtained by multiplying and integrating the known desired spectrum (either blackbody or polystyrene) with the spectral response of the QDIP at the prescribed bias. The desired spectra were measured with a Nicolet Fourier-transform infrared spectrometer with  $4\text{-cm}^{-1}$  resolution in the wavelength range  $2.5\text{--}20 \mu\text{m}$ . After the QDIP photocurrents were predicted for each applied bias, a reconstructed photocurrent, corresponding to each multispectral filter (band) was constructed by linearly combining the QDIP photocurrents according to the weights corresponding to each desired multispectral band (as computed in the projection step of the algorithm).

The results for the hyperspectral-sensing mode are presented in Fig. 9, along with actual spectra measured by the Fourier-transform infrared device. We used triangular filters of desired FWHM of  $0.5 \mu\text{m}$  and  $0.25 \mu\text{m}$ . As might be expected, the procedure yields very good results in reconstructing the blackbody spectrum, especially with triangular filters of parameter  $0.5 \mu\text{m}$  [Fig. 9(a)]. With a desired FWHM of  $0.25 \mu\text{m}$ , however, the approximation has some spurious perturbations that are especially visible between  $7$  and  $8 \mu\text{m}$ , as shown in Fig. 9(c). Note that as the blackbody spectrum is a slowly varying function of

wavelength, and the relatively broad hyperspectral filter ( $0.5 \mu\text{m}$ ) does not adversely affect the hyperspectral spectrum. On the other hand, the polystyrene spectrum has both large-scale spectral features and narrow absorption lines. We therefore see that the hyperspectral data capture the overall envelope of the spectrum but do not resolve spectral features narrower than the realized resolution of the bands ( $0.5 \mu\text{m}$ ), as seen in Fig. 9(b). Notably, the hyperspectral data are able to resolve the  $\text{H}_2\text{O}$  and  $\text{CO}_2$  absorption features between  $3.5$  and  $4 \mu\text{m}$ , when filters with a FWHM of  $0.25 \mu\text{m}$  are employed, as shown with arrows in Fig. 9(d). Note that, even though the fine spectral structure of the polystyrene film was not resolved, the hyperspectral-sensor data clearly indicate that there are important differences in the spectra of the blackbody and that of the polystyrene film. This information may not be as detailed as that obtained with a high-resolution spectrometer, but it is adequate to indicate that a second material is present and demonstrates the power of the proposed postprocessing technique and its potential utility as an algorithm-based spectrometer.

To put the hyperspectral data offered by our postprocessing technique in better perspective, we generated Fig. 10, where two, “bad” and “good,” representative triangular-filter approximations are shown. The base-width of the triangle is  $1.0 \mu\text{m}$  (which corresponds to a desired FWHM of  $0.5 \mu\text{m}$ ) and for which the centers are at



4.0  $\mu\text{m}$  and 7.65  $\mu\text{m}$  for Figs. 10(a) and 10(b), respectively. Note that the yielded postprocessing FWHM is approximately 1.0  $\mu\text{m}$ , which is twice as much as the desired FWHM. By our observations from all the approximations and also from Fig. 7(b), FWHM of  $\sim 0.5$   $\mu\text{m}$  is near the limit of the algorithm, depending on the center wavelength of the filter to be approximated. The use of a desired FWHM of 0.5  $\mu\text{m}$  is partially successful in capturing finer spectral details. However, this comes at the expense, at some wavelengths, of reduced ability to have an isolated peak and of finding the peak in the approximation. The approximations and the reconstructions become more noisy and less dependable as we force the FWHM below 0.5  $\mu\text{m}$ . For example, if we force the desired FWHM to 0.25  $\mu\text{m}$ , as shown in Fig. 11(a), then we not only observe that the main peak becomes wider, but we also start to see the emergence of spurious competing peaks. One possible remedy to the spurious peaks problem is to define a measure (such as the ratio between the main peak and the first competing peak) that can be incorporated in the penalization in Eq. (9).

The results for the two multispectral modes are presented in Tables 2 and 3. For the desired parameters in Table 1, the actual values of the spectra, the reconstructed spectra obtained by ideal (triangular) filters, and

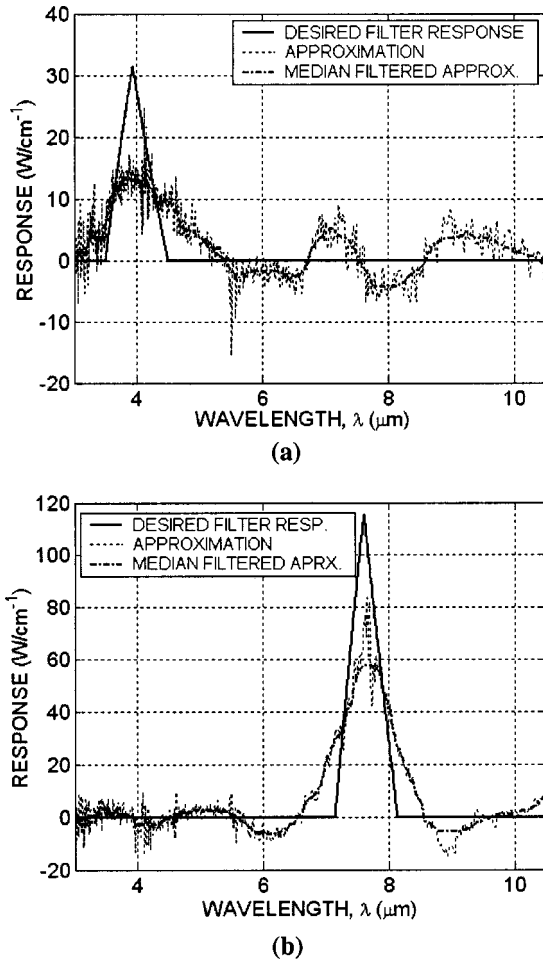


Fig. 10. Example filter approximation: triangular filters with a desired FWHM of 0.5  $\mu\text{m}$  and with centers of (a) 4.0  $\mu\text{m}$  (a bad approximation) and (b) 7.65  $\mu\text{m}$  (a good approximation).

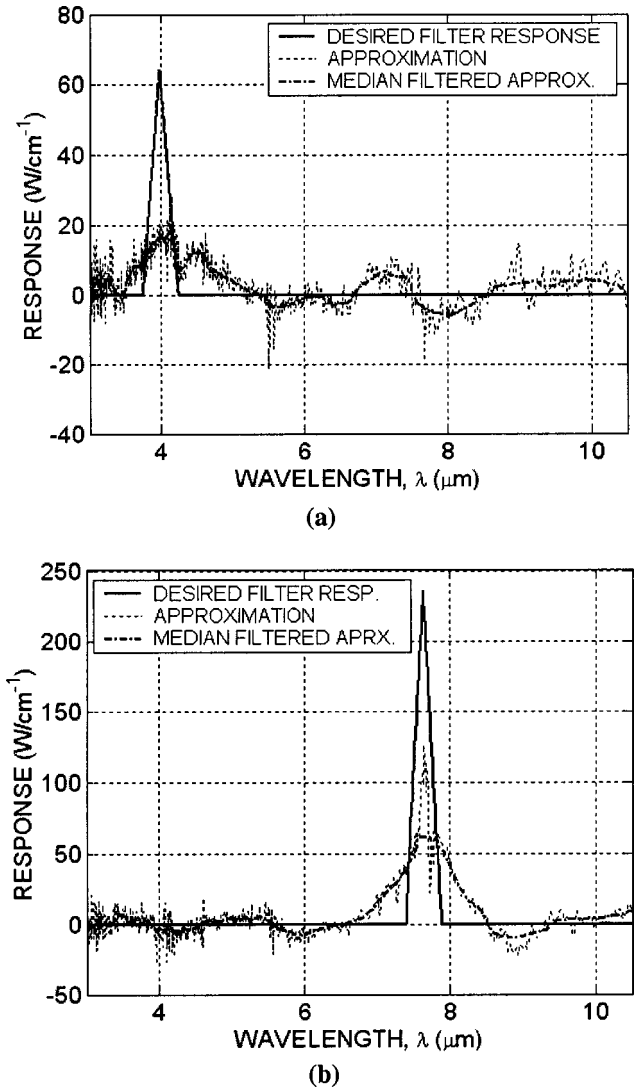


Fig. 11. Example filter approximation: triangular filters with a desired FWHM of 0.25  $\mu\text{m}$  and centers of (a) 4.0  $\mu\text{m}$  (a bad approximation) and (b) 7.65  $\mu\text{m}$  (a good approximation).

the reconstructed spectra obtained by approximated filters, are shown together for comparison. At these multispectral settings, with much wider spectral resolutions, the QDIP can realize spectra that are excellent approximations to the desired spectra. We see from the data in Tables 2 and 3 that both multispectral modes can be used to easily differentiate the polystyrene spectrum from the blackbody spectrum. The two modes were chosen to demonstrate one system with broad spectral coverage and uniform bands and a second system with variable spectral coverage and bandwidths. These two examples reinforce the full adaptivity of the QDIP sensors. We also see that the reconstruction obtained by either the ideal or approximated spectra are very close, which means that the limitation in accuracy of the reconstruction stems from the mathematical limitation. Even if we use ideal filters (in this case, with parameter 0.5), the ideal filter is not thin enough to resolve the fine parts of the target spectra. Theoretically, we have to have infinitesimally thin filters (delta function) to reconstruct the spectra perfectly.

**Table 2. Seven-Band Multispectral Reconstruction**

Center ( $\mu\text{m}$ )	Actual	Ideal	Approximation
Reconstruction of 3.0-mm polystyrene filter spectrum ( $\text{W}/\text{cm}^{-1}$ )			
4.0	0.6887	0.6073	0.5969
5.0	0.7905	0.7391	0.7358
6.0	0.6211	0.5657	0.5753
7.0	0.3315	0.3705	0.3920
8.0	0.5330	0.3529	0.3349
9.0	0.5745	0.4791	0.5080
10.0	0.2967	0.4019	0.3958
Reconstruction of blackbody spectrum (normalized) ( $\text{W}/\text{cm}^{-1}$ )			
4.0	0.7029	0.6926	0.6807
5.0	0.8484	0.8548	0.8510
6.0	0.9532	0.9420	0.9580
7.0	0.9994	0.9525	1.0077
8.0	0.9881	1.0280	0.9753
9.0	0.9012	0.8672	0.9194
10.0	0.8452	0.8709	0.8575

**Table 3. Three-Band Multispectral Reconstruction**

Center ( $\mu\text{m}$ )	Actual	Ideal	Approximation
Reconstruction of 3.0-mm polystyrene filter spectrum ( $\text{W}/\text{cm}^{-1}$ )			
5.0	0.6887	0.7244	0.7133
7.5	0.2758	0.3330	0.3223
9.5	0.3840	0.4340	0.4478
Reconstruction of blackbody spectrum (normalized) ( $\text{W}/\text{cm}^{-1}$ )			
5.0	0.8424	0.8424	0.8296
7.5	0.9998	1.0271	0.9940
9.5	0.8669	0.8599	0.8872

### B. Further Comments on the Algorithm Implementation

All the reconstruction was done by use of the regularization parameter  $\alpha = 0.04$ , as it appeared to give the best results. If too large an  $\alpha$  parameter is used, then our reconstruction loses resolution, since the penalty on fluctuations is increased [see Eq. (9)]. If we use too small an  $\alpha$ , then the reconstruction becomes very noisy, which results in noisy FWHM measurement, shift of the peak due to the noise, and therefore a poor and erroneous reconstruction. By itself, penalizing the noise is not enough. We had to use a median filter to smoothen the reconstructed algorithm in order to be able to find measure FWHM consistently. The median-filtered spectral response was not, however, used in the reconstruction of  $\hat{Y}$  in Eq. (1). The filtering was solely used to obtain an accurate estimate of the yielded FWHM. In the bias-dependent response measurements (between 3 and 11  $\mu\text{m}$ ), we had 1257 data points, and the length of the median filter was chosen to be 50 ( $\sim 4\%$  of the mesh size), which provided good results in terms of measuring the FWHM.

Other manifestations of roughness/noise penalization and filter shapes (instead of a triangular shape, for example) can be used in order to generate better approximations in the projection step, which may further improve

the overall performance of the algorithm. We are currently pursuing a number of strategies to this effect.

## 5. CONCLUSIONS

We have presented a new spectrally adaptive infrared photodetector technology based on bias-tunable quantum-dot technology. The QD detectors have broad spectral responses that are seen to shift toward longer wavelengths as the bias is increased. While the broad response of the photodetectors is not alone enough to provide spectral adaptivity, we have combined these detectors with a post-processing strategy that allows the spectral response to be tuned by linearly combining the response of the QDIPs at a number of different biases. By altering the weights used in this combination, the center wavelength and bandwidth can be independently tuned. These sensors have the ability to simultaneously perform a number of spectral-sensing missions, including broadband infrared imagery, adaptive two-color imagery, adaptive multispectral imagery, and low-resolution hyperspectral imagery.

We are currently able to improve the spectral resolution of the QDIPs by a factor of  $\sim 4$ , and we have realized tunable sensitivity with 0.5- $\mu\text{m}$  resolution from 4 to 10  $\mu\text{m}$ . With improved spectral responses from the individual QDIPs, the performance of the entire system will improve, especially in hyperspectral applications.

## REFERENCES

1. J. M. Arias, M. Zandian, J. G. Pasko, J. Bajaj, L. J. Kozlowski, W. E. Tennant, and R. E. DeWames, "MBE HgCdTe infrared focal plane array (IRFPA) flexible manufacturing," in *Infrared Detectors: State of the Art II*, R. E. Longshore, ed., Proc. SPIE **2274**, 2–16 (1994).
2. P. Tribolet, J. P. Chatard, P. Costa, and A. Manissadjian, "Progress in HgCdTe homojunction infrared detectors," J. Cryst. Growth **184–185**, 1262–1271 (1998).
3. J. M. Arias, M. Zandian, J. Bajaj, J. G. Pasko, L. O. Bubulac, S. H. Shin, and R. E. DeWames, "Molecular beam epitaxy HgCdTe growth-induced void defects and their effect on infrared photodiodes," J. Electron. Mater. **24**, 521–524 (1995).
4. R. M. Biefeld, J. R. Wendt, and S. R. Kurtz, "Improving the performance of  $\text{InAs}_{1-x}\text{Sb}_x/\text{InSb}$  infrared detectors grown by metalorganic chemical vapor deposition," J. Cryst. Growth **107**, 836–839 (1991).
5. M. H. Young, D. H. Chow, A. T. Hunter, and R. H. Miles, "Recent advances in  $\text{Ga}_{1-x}\text{In}_x\text{Sb}/\text{InAs}$  superlattice IR detector materials," Appl. Surf. Sci. **123–124**, 395–399 (1998).
6. L. West and S. Eglash, "First observation of an extremely large-dipole infrared transition within the conduction band of a GaAs quantum well," Appl. Phys. Lett. **46**, 1156–1158 (1985).
7. B. F. Levine, "Quantum-well infrared photodetectors," J. Appl. Phys. **74**, R1–R81 (1993).
8. A. C. Goldberg, J. W. Little, S. W. Kennerly, D. W. Beekman, and R. P. Leavitt, "Temperature dependence of the responsivity of quantum well infrared photodetectors," in *Proceedings of 6th International Symposium on LWIR Detectors and Arrays: Physics and Applications*, S. S. Li, M. Z. Tidrow, S. D. Gunapala, and H. C. Liu, eds. (Electrochemical Society, Boston, Mass., 1999), Vol. 98-21, pp. 122–123.
9. C. J. Chen, K. K. Choi, W. H. Chang, and D. C. Tsui, "Two-color corrugated quantum-well infrared photodetector for remote temperature sensing," Appl. Phys. Lett. **72**, 7–9 (1998).
10. S. D. Gunapala and K. M. S. V. Bandara, "Recent developments in quantum well infrared photodetectors," in *Thin*

- Films*, M. H. Francombe and J. L. Vossen, eds. (Academic, New York, 1995), pp. 113–237.
11. M. Z. Tidrow, J. C. Chirefflang, S. S. Li, and K. Bacher, “A high strain two-stack two-color quantum well infrared photodetector,” *Appl. Phys. Lett.* **70**, 859–861 (1997).
  12. V. Ryzhii, I. Khmyrova, V. Mitin, M. Strosio, and M. Willander, “On the detectivity of quantum-dot infrared photodetectors,” *Appl. Phys. Lett.* **78**, 3523–3525 (2001).
  13. M. A. Kinch, “Fundamental physics of infrared detector materials,” *J. Electron. Mater.* **29**, 809–817 (2000).
  14. A. Rogalski, “Assessment of HgCdTe photodiodes and quantum well infrared photoconductors for long wavelength focal plane arrays,” *Infrared Phys. Technol.* **40**, 279–294 (1999).
  15. J. Phillips, P. Bhattacharya, S. W. Kennerly, D. W. Beekman, and M. Dutta, “Self-assembled InAs-GaAs quantum-dot intersubband detectors,” *IEEE J. Quantum Electron.* **35**, 936–943 (1999).
  16. H. C. Liu, M. Gao, J. McCaffrey, Z. R. Wasilewski, and S. Fafard, “Quantum dot infrared photodetectors,” *Appl. Phys. Lett.* **78**, 79–81 (2001).
  17. S. Raghavan, P. Rotella, A. Stintz, B. Fuchs, S. Krishna, C. Morath, D. A. Cardimona, and S. W. Kennerly, “High-responsivity, normal-incidence long-wave infrared ( $\lambda \sim 7.2 \mu\text{m}$ ) InAs/In<sub>0.15</sub>Ga<sub>0.85</sub>As dots-in-a-well detector,” *Appl. Phys. Lett.* **81**, 1369–1371 (2002), and references therein.
  18. P. Bhattacharya, S. Krishna, J. Phillips, P. J. McCann, and K. Namjou, “Carrier dynamics in self-organized quantum dots and their application to long-wavelength sources and detectors,” *J. Cryst. Growth* **227**, 27–35 (2001).
  19. P. Bhattacharya, S. Krishna, J. D. Phillips, D. Klotzkin, and P. J. McCann, “Quantum dot carrier dynamics and far-infrared devices,” in *Optoelectronic Materials and Devices II*, Y.-K. Su and P. Bhattacharya, eds., *Proc. SPIE* **4078**, 84–89 (2000).
  20. V. Ryzhii, M. Ershov, I. Khmyrova, M. Ryzhii, and T. Iizuka, “Multiple quantum-dot infrared phototransistors,” *Physica B* **227**, 17–20 (1996).
  21. M. R. Descour, C. E. Volin, E. L. Dereniak, T. M. Gleeson, M. F. Hopkins, D. W. Wilson, and P. D. Maker, “Demonstration of a computed-tomography imaging spectrometer using a computer-generated hologram disperser,” *Appl. Opt.* **36**, 3694–3698 (1997).
  22. A. C. Goldberg, T. Fischer, and Z. I. Derzko, “Application of dual band infrared focal plane arrays to tactical and strategic military problems,” in *Infrared Technology and Applications XVIII*, B. Andersen, G. F. Fulop, and M. Stronik, eds., *Proc. SPIE* **4480**, 500–514 (2002).
  23. F. E. Prins, G. Lehr, M. Burkad, S. Nikitin, H. Schweizer, and G. Smith, “Quantum dots and quantum wires with high optical quality by implantation-induced intermixing,” *Jpn. J. Appl. Phys., Part 1* **32**, 6228–6232 (1993).
  24. D. Bimberg, M. Grundmann, and N. N. Ledentsov, *Quantum Dot Heterostructures*, 1st ed. (Wiley, New York, 1999).
  25. L. F. Lester, A. Stintz, H. Li, T. C. Newell, E. A. Pease, B. A. Fuchs, and K. J. Malloy, “Optical characteristics of 1.24- $\mu\text{m}$  InAs quantum-dot laser diodes,” *IEEE Photon. Technol. Lett.* **11**, 931–933 (2000), and references therein.
  26. E.-T. Kim, Z. Chen, and A. Madhukar, “Selective manipulation of InAs quantum dot electronic states using a lateral potential confinement layer,” *Appl. Phys. Lett.* **81**, 3473–3475 (2002).
  27. S. Krishna, P. Rotella, S. Raghavan, A. Stintz, M. M. Hayat, S. J. Tyo, and S. W. Kennerly, “Bias-dependent tunable response of normal incidence long wave infrared quantum dot detectors,” in *Proceedings of IEEE/LEOS Annual Meeting* (Institute of Electrical and Electronics Engineers, New York, 2002), Vol. 2, pp. 754–755.
  28. H. Stark and J. Woods, *Probability and Random Processes with Applications to Signal Processing*, 3rd ed. (Prentice-Hall, Englewood Cliffs, N.J., 2002).
  29. J. Luenberger, *Optimization by Vector Space Methods* (Wiley, New York, 1967).
  30. P. Rotella, S. Raghavan, A. Stintz, B. Fuchs, S. Krishna, C. Morath, D. Le, and S. W. Kennerly, “Normal incidence InAs/InGaAs dots-in-well detectors with current blocking AlGaAs layer,” *J. Cryst. Growth* **251**, 787–793 (2003).
  31. G. V. Winckel and S. Krishna, “A theoretical model for bias dependent shift of absorption spectra in quantum well infrared photodetectors,” in *Proceedings of IEEE/LEOS Annual Meeting* (Institute of Electrical and Electronics Engineers, New York, 2002), Vol. 2, pp. 756–757.